9. M. Sawamura, H. Iikura, E. Nakamura, *J. Am. Chem. Soc.* **118**, 12850 (1996).
10. M. Sawamura, H. Iikura, T. Ohama, U. E. Hackler, E. Nakamura, *J. Organometal. Chem.* **599**, 32 (2000).
11. M. Sawamura, M. Toganoh, Y. Kuninobu, S. Kato, E. Nakamura, *Chem. Lett.* (no. 3), 270 (2000).
12. M. Sawamura, H. Iikura, A. Hirai, E. Nakamura, *J. Am. Chem. Soc.* **120**, 8285 (1998).
13. M. Sano, K. Oishi, T. Ishi-i, S. Shinkai, *Langmuir* **8**, 3773 (2000).
14. H. Iikura, S. Mori, M. Sawamura, E. Nakamura, *J. Org. Chem.* **62**, 7912 (1997).
15. S. W. Provencher, *Makromol. Chem.* **180**, 201 (1979).
16. B. Burchard, M. Schmidt, W. H. Stockmayer, *Macromolecules* **13**, 580 (1980).
17. M. Sawamura *et al.*, *Chem. Lett.* (no. 9), 1098 (2000).
18. M. Matsumoto *et al. Langmuir* **11**, 660 (1995).
19. E. Nakamura *et al., Angew. Chem. Int. Ed. Engl.* **39**, 4254 (2000).
20. Supported by NSF grant DMR 9984102 and DOE grant DEFG0286ER45237.016 (B.C.), by a Feodor-Lynen Fellowship from the Alexander von Humboldt Foundation (C.B.), and by a Monbusho Grant-in-Aid for Scientific Research on Priority Area (Innovative Synthetic Reactions) and the Japan Society for the Promotion of Science–NSF Exchange Program.

21 November 2000; accepted 8 February 2001

Nanobelts of Semiconducting Oxides

Zheng Wei Pan,[1] Zu Rong Dai,[1] Zhong Lin Wang[1,2]*

Ultralong beltlike (or ribbonlike) nanostructures (so-called nanobelts) were successfully synthesized for semiconducting oxides of zinc, tin, indium, cadmium, and gallium by simply evaporating the desired commercial metal oxide powders at high temperatures. The as-synthesized oxide nanobelts are pure, structurally uniform, and single crystalline, and most of them are free from defects and dislocations. They have a rectanglelike cross section with typical widths of 30 to 300 nanometers, width-to-thickness ratios of 5 to 10, and lengths of up to a few millimeters. The beltlike morphology appears to be a distinctive and common structural characteristic for the family of semiconducting oxides with cations of different valence states and materials of distinct crystallographic structures. The nanobelts could be an ideal system for fully understanding dimensionally confined transport phenomena in functional oxides and building functional devices along individual nanobelts.

Binary semiconducting oxides, such as ZnO, SnO_2, In_2O_3, and CdO, have distinctive properties and are now widely used as transparent conducting oxide materials (*1*) and gas sensors (*2*). For example, fluorine-doped SnO_2 film is widely used in architectural glass applications because of its low emissivity for thermal infrared heat (*1*). SnO_2 nanoparticles are regarded as one of the most important sensor materials for detecting leakage of several inflammable gases owing to their high sensitivity to low gas concentrations (*2*). Tin-doped indium oxide (In_2O_3:Sn, ITO) film is an ideal material for flat panel displays because of its high electrical conductivity and high optical transparency (*1*), and ZnO is regarded as an ideal alternative material for ITO because of its lower cost and easier etchability (*1*). The current studies of semiconducting oxides have been focused on two-dimensional films and zero-dimensional nanoparticles, which can be readily synthesized with various well-established techniques such as sputtering (for films) and sol-gel (for particles). In contrast, investigations of wirelike semiconducting oxide nanostructures are cumbersome because of the unavailability of nanowire structures.

As stimulated by the novel properties of carbon nanotubes, wirelike nanostructures have attracted extensive interest over the past decade because of their great potential for addressing some basic issues about dimensionality and space-confined transport phenomena as well as applications (*3*). Besides nanotubules (*4*, *5*), many other wirelike nanomaterials, such as carbides [SiC (*6*–*8*) and TiC (*6*)], nitrides [GaN (*9*, *10*) and Si_3N_4 (*11*)], compound semiconductors (*12*, *13*), element semiconductors [Si (*14*–*16*) and Ge (*14*)], and oxide [Ga_2O_3 (*17*) and MgO (*18*)] nanowires, have been successfully fabricated. In geometrical structures, these nanostructures can be classified into two main groups: hollow nanotubes and solid nanowires, which have a common characteristic of cylindrical symmetric cross section. Here, we report another group of distinctly different semiconducting oxide nanostructures that have a rectangular cross section, in correspondence to a beltlike (or ribbonlike) morphology. The oxides with the nanobelt morphology cover cations with different valence states and materials with different crystallographic structures, and it seems to be a common structural characteristic for the family of semiconducting oxides.

Our synthesis is based on thermal evaporation of oxide powders under controlled conditions without the presence of catalyst (*19*). The desired oxide powders were placed at the center of an alumina tube that was inserted in a horizontal tube furnace, where the temperature, pressure, and evaporation time were controlled. In our experiments, except for the evaporation temperature, which was determined on the basis of the melting point of the oxides used, we kept the following parameters constant: evaporation time, 2 hours; chamber pressure, 300 torr; and Ar flowing rate, 50 standard cubic centimeters per minute. During evaporation, the products were deposited onto an alumina plate placed at the downstream end of the alumina tube. The as-deposited products were characterized and analyzed by x-ray diffraction (XRD) (Philips PW 1800 with Cu Kα radiation), scanning electron microscopy (SEM) (Hitachi S800 FEG), transmission electron microscopy (TEM) [Hitachi HF-2000 FEG at 200 kV and JEOL 4000EX high-resolution TEM (HRTEM) at 400 kV], and energy-dispersive x-ray spectroscopy (EDS).

Thermal evaporation of ZnO powders (purity: 99.99%; melting point: 1975°C) at 1400°C for 2 hours resulted in white woollike products that formed in high yield on the surface of the alumina plate. SEM observations reveal that the products consist of a large quantity of wirelike nanostructures with typical lengths in the range of several tens to several hundreds of microm-

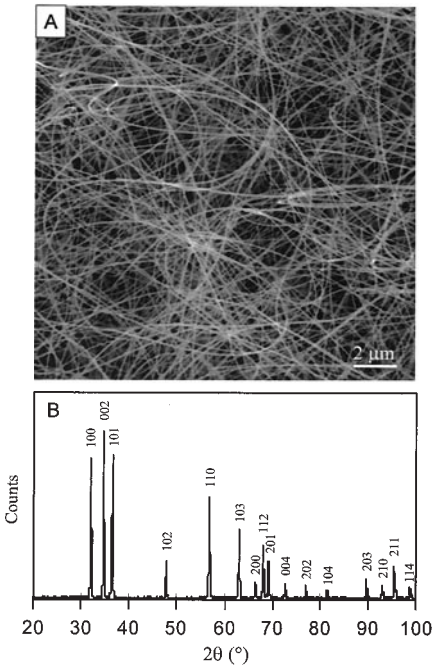

Fig. 1. Ultralong nanobelt structure of ZnO (with wurtzite crystal structure). (**A**) SEM image of the as-synthesized ZnO nanobelts obtained from thermal evaporation of ZnO powders at 1400°C. (**B**) XRD pattern recorded from the ZnO nanobelts.

[1]School of Materials Science and Engineering, [2]School of Chemistry and Biochemistry, Georgia Institute of Technology, Atlanta, GA 30332–0245, USA.

*To whom correspondence should be addressed. E-mail: zhong.wang@mse.gatech.edu

eters; some of them even have lengths on the order of millimeters (Fig. 1A). EDS microanalysis and powder XRD measurement (Fig. 1B) show that the sample is wurtzite (hexagonal) structured ZnO with lattice constants of a = 3.249 Å and c = 5.206 Å, consistent with the standard values for bulk ZnO (*20*).

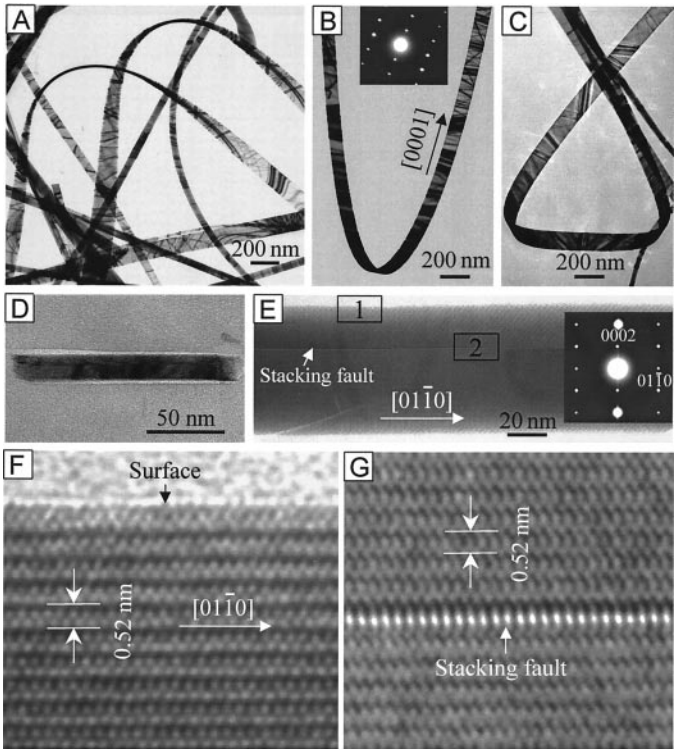

Fig. 2. TEM and HRTEM images of ZnO nanobelts showing their geometrical shape. (**A** to **C**) TEM images of several straight and twisted ZnO nanobelts, displaying the shape characteristics of the belts. (**D**) Cross-sectional TEM image of a ZnO nanobelt, showing a rectanglelike cross section with width-to-thickness ratio of ~9. The cross-sectional TEM specimen was prepared by slicing nanobelts embedded in epoxy with an ultramicrotone. (**E**) TEM image of a nanobelt growing along [01$\bar{1}$0], showing only one stacking fault present in the nanobelt; this type of nanobelt is the only one that has a defect. The inset shows the electron diffraction pattern. (**F**) HRTEM image from box 1 in (E), showing a clean and structurally perfect surface (the amorphous contrast seen above the surface is from the amorphous carbon film used to support the nanobelt for TEM imaging). (**G**) HRTEM image from box 2 in (E), showing the stacking fault.

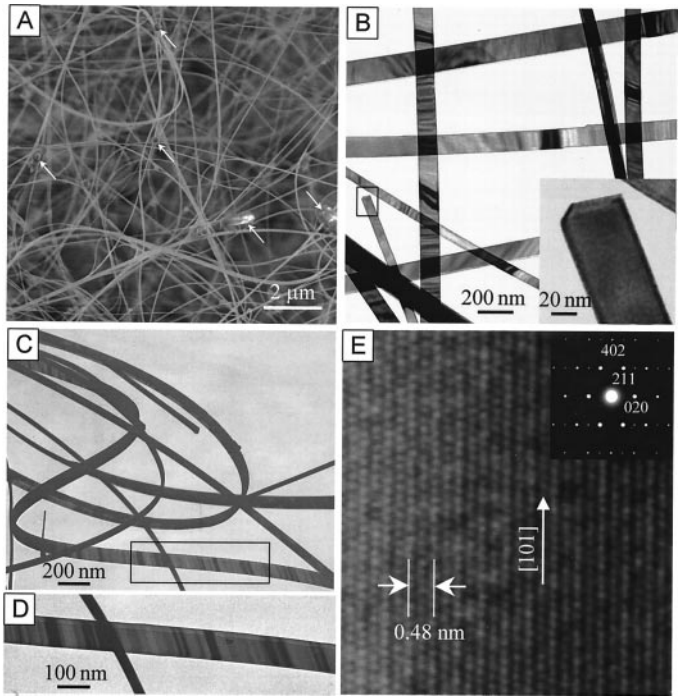

Fig. 3. Superlong nanobelt structure of SnO_2 (with rutile crystal structure). (**A**) SEM image of the as-synthesized SnO_2 nanobelts, showing a high volume percentage (> 95%) of SnO_2 nanobelts and a small amount of Sn nanoparticles as indicated by arrows. (**B** to **D**) TEM images of SnO_2 nanobelts with straight and twisted shapes. An enlargement of a broken nanobelt is inserted in (B) to display the rectanglelike cross section of the belt. The beltlike shape is further verified by an enlargement of the boxed region in (C) as redisplayed in (D); the width-to-thickness ratio is ~5. (**E**) HRTEM image of a SnO_2 nanobelt showing that the nanobelt is single crystalline and free from dislocation and defects. (Inset) The corresponding electron diffraction pattern recorded with electron beam perpendicular to the long axis of a belt, showing the growth direction to be [101] (note the rutile structure of the sample). The SnO_2 nanobelts shown in (A), (B), and (E) were obtained from thermal evaporation of SnO_2 powders at 1350°C; the SnO_2 nanobelts shown in (C) and (D) were obtained from thermal evaporation of SnO powders at 1000°C, but they preserve the same crystal structure and same growth morphology.

TEM images reveal that the geometrical shape of the ZnO nanostructures is a belt (Fig. 2, A to C) that is distinct in cross section from the previously reported nanotubes (*4*, *5*) and nanowires (*6*–*18*). Each nanobelt has a uniform width along its entire length, and the typical widths of the nanobelts are in the range of 50 to 300 nm. No particle was observed at the ends of the nanobelts. A ripplelike contrast observed in the TEM image is due to strain resulting from the bending of the belt. To further verify the morphological characteristic of the ZnO nanobelts, a cross-sectional TEM image taken from a nanobelt is given in Fig. 2D, which exhibits a rectanglelike cross section. The typical thickness and width-to-thickness ratios of the ZnO nanobelts are in the range of 10 to 30 nm and ~5 to 10, respectively, as determined from several tens of nanobelts. HRTEM and electron diffraction show that the ZnO nanobelts are structurally uniform and single crystalline but with two different growth directions. The nanobelt, growing along [0001] and enclosed by $\pm(2\bar{1}\bar{1}0)$ and $\pm(01\bar{1}0)$ facets, shows no defect and no dislocation; the one growing along [01$\bar{1}$0] and enclosed by $\pm(0001)$ and $\pm(2\bar{1}\bar{1}0)$ facets is also dislocation free but with only a single stacking fault that is parallel to the axis and runs through out the entire length of the nanobelt (Fig. 2, E and G). The surfaces of the nanobelts are clean, atomically sharp, and without any sheathed amorphous phase (Fig. 2F).

The beltlike geometrical morphology is a common structural characteristic for functional oxides with different crystallographic structures, at least for the ones we studied. For example, single crystalline SnO_2 nanobelts of rutile structure can consistently be synthesized by thermal evaporation of either SnO_2 powders (purity: 99.9%; melting point: 1630°C) at 1350°C or SnO powders (purity: 99.9%; melting point: 1080°C) at 1000°C. After evaporation, similar white fuzzlike products were deposited on the alumina plate, whether the source material was SnO_2 or SnO. SEM imaging (Fig. 3A) and EDS analysis show that the products are composed of large quantities of ultralong SnO_2 nanobelts (with lengths up to on the order of millimeters) and a small fraction of Sn nanoparticles (as indicated by arrows in Fig. 3A) (*21*). XRD patterns from the as-synthesized nanobelt samples show the rutile type structure with lattice constants of a = 4.722 Å and c = 3.184 Å, which are consistent with those of bulk SnO_2 (*20*). TEM images (Fig. 3, B to D) display the characteristic shape of the SnO_2 nanobelts (note the rectanglelike cross section of a broken nanobelt in Fig. 3B and a side view of a nanobelt displayed in Fig. 3D). The ripplelike strain contrast can also be seen in SnO_2 nanobelts. Each nanobelt is uniform in width and thickness, and the typical widths of the SnO_2 nanobelts are in the range of 50 to 200 nm. Cross-sectional TEM

observations show that the cross sections of the SnO_2 nanobelts are rectanglelike, with typical width-to-thickness ratios of ~5 to 10. An HRTEM image (Fig. 3E) reveals that the nanobelts are single crystalline and dislocation free. The electron diffraction pattern (inset in Fig. 3E) indicates that the SnO_2 nanobelt grows along [101] and it is enclosed by ±(010) and ±(10$\bar{1}$) crystallographic facets.

Nanobelts of In_2O_3 with C–rare earth crystal structure (*20*) were also synthesized by our method (Fig. 4A). The evaporation of In_2O_3 powders (purity: 99.99%; melting point: ~1920°C) at 1400°C yields In_2O_3 nanobelts. TEM observations show that most of the In_2O_3 nanobelts have uniform width and thickness along their lengths (Fig. 4B). However, some nanobelts exhibit a sharp shrinkage in width while the thickness is preserved and form a bridgelike structure (Fig. 4C), which may be a candidate for transport measurement from an oxide nanobridge. Typically, the In_2O_3 nanobelts have widths in the range of 50 to 150 nm and lengths of several tens to several hundreds of micrometers. Electron diffraction (inset, Fig. 4B) analysis shows that the In_2O_3 nanobelts are single crystalline and grow along ⟨100⟩, the surfaces being enclosed by {100}.

Nanobelts of CdO with NaCl cubic structure (*20*) were also synthesized by evaporating CdO powders (purity: 99.998%; melting point: 1430°C) at 1000°C. Besides CdO nanobelts, many single crystalline CdO sheets with sizes on the order of several to several tens of micrometers were also formed (Fig. 4D). These CdO sheets usually have such shapes as rectangle, triangle, and parallelogram. The lengths of the CdO nanobelts are usually less than 100 μm, and their widths are typically 100 to 500 nm (Fig. 4, E and F), substantially wider and shorter than those of ZnO, SnO_2, and In_2O_3 nanobelts. As a result, the width-to-thickness ratios of CdO nanobelts are usually greater than 10. The electron diffraction pattern (inset in Fig. 4F) shows that the nanobelts grow along [100] and their surfaces are enclosed by ±(001) and ±(010) facets. The symmetry patterns observed in the bright-field TEM images (Fig. 4F) are the bending contour in electron diffraction due to the bending of the nanobelt (*22*). Some nanobelts were broken into two halves (Fig. 4G) during TEM observation because of electron beam illumination, which is likely to be caused by the easy cracking characteristic of the NaCl-type ionic structure of the nanobelt. Thus, it may be possible to cut these nanobelts with a focused electron or ion beam, so that nanobelts with specific lengths for nanodevice applications could be fabricated.

Our studies also demonstrated that, besides the above-mentioned four oxides that were usually regarded as the transparent conducting oxides, the beltlike nanostructures were also obtained from other oxide materials, such as Ga_2O_3 (*23*) and PbO_2.

Our TEM analysis shows that the growth of the nanobelts may not be dominated by the vapor-liquid-solid (VLS) process (*24*) proposed for the nanowires grown by a catalytic-assisted technique (*12–14*, *25*), in which a metal particle is located at the growth front of the wire and acts as the catalytic active site. Because the only source material used in our synthesis is pure oxide powders and the composition of the oxide nanobelts is similar or identical to the starting oxide, it is likely that the growth is governed by a vapor-solid process (*18*, *26*), in which the oxide vapor, evaporated from the starting oxide at a higher temperature zone, directly deposits on a substrate at a lower temperature region and grows into beltlike nanostructures.

The beltlike morphology is distinct from those of semiconductor nanowires. With a well-defined geometry and perfect crystallinity, the semiconducting oxide nanobelts are likely to be a model materials family for a systematic experimental and theoretical understanding in the fundamental electrical, thermal, optical, and ionic transport processes in wirelike nanostructures with the absence of dislocations and defects. The semiconducting oxide nanobelts could be doped with different elements and used for fabricating nanosize sensors based on the characteristics of individual nanobelts.

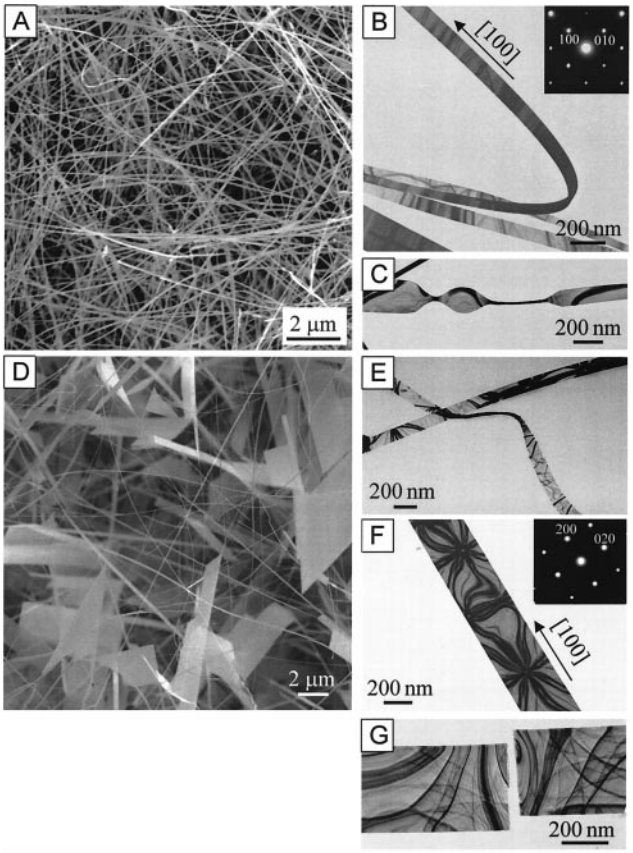

Fig. 4. Ultralong, high-purity nanobelts of (**A** to **C**) In_2O_3 (with C–rare earth crystal structure) and (**D** to **G**) CdO (with NaCl cubic crystal structure). (A) SEM image of the as-synthesized In_2O_3 nanobelts. (B) TEM image of the In_2O_3 nanobelts and an electron diffraction pattern (inset), showing the single crystalline, defect-free structure of the nanobelts. The nanobelts grow along [100]. (C) A nanobelt with an abruptly reduced width. This structure is frequently observed for In_2O_3. (D) SEM image of the as-synthesized CdO nanobelts and sheets. (E and F) TEM images and a corresponding electron diffraction pattern of the single crystalline CdO nanobelts growing along [100]. (G) A broken CdO nanobelt as a result of focused electron beam illumination.

References and Notes

1. D. S. Ginley, C. Bright, *Mater. Res. Soc. Bull.* **25**, 15 (2000).
2. N. Yamazoe, *Sens. Actuators B* **5**, 7 (1991).
3. C. Dekker, *Phys. Today* **52**, 22 (1999).
4. S. Iijima, *Nature* **354**, 56 (1991).
5. Y. Feldman, E. Wasserman, D. J. Srolovitz, R. Tenne, *Science* **267**, 222 (1995).
6. H. J. Dai *et al.*, *Nature* **375**, 769 (1995).
7. Z. W. Pan *et al.*, *Adv. Mater.* **12**, 1186 (2000).
8. Z. L. Wang *et al.*, *Appl. Phys. Lett.* **77**, 3349 (2000).
9. W. Han, S. Fan, Q. Li, Y. Hu, *Science* **277**, 1287 (1997).
10. X. F. Duan, C. M. Lieber, *J. Am. Chem. Soc.* **122**, 188 (2000).
11. W. Q. Han *et al.*, *Appl. Phys. Lett.* **71**, 2271 (1997).
12. X. F. Duan, C. M. Lieber, *Adv. Mater.* **12**, 298 (2000).
13. X. F. Duan, Y. Huang, Y. Cui, J. Wang, C. M. Lieber, *Nature* **409**, 66 (2001).
14. A. M. Morales, C. M. Lieber, *Science* **279**, 208 (1998).
15. S. T. Lee, N. Wang, Y. F. Zhang, Y. H. Tang, *Mater. Res. Soc. Bull.* **24**, 36 (1999).
16. D. P. Yu *et al.*, *Solid State Commun.* **105**, 403 (1998).
17. H. Z. Zhang *et al.*, *Solid State Commun.* **109**, 677 (1999).
18. P. Yang, C. M. Lieber, *J. Mater. Res.* **12**, 2981 (1997).
19. A provisional patent has been filed by Georgia Tech Research Cooperation.
20. F. S. Galasso, *Structure and Properties of Inorganic Solids* (Pergamon, New York, 1970).
21. The Sn nanoparticles are adhered on the surfaces of the belts rather than at the ends, in contrast to the nanowires prepared by VLS reaction (*12–14*) that always terminate at one end with a catalytic nanoparticle. The formation of the Sn nanoparticles is believed to be related to the decomposition of the SnO_2 or SnO vapor.
22. P. B. Hirsch, A. Howie, R. B. Nicholson, D. W. Pashley, M. L. Whelan, *Electron Microscopy of Thin Crystals* (Krieger, New York, 1977).
23. The Ga_2O_3 nanobelts can be prepared by either heating mixed Ga−Ga_2O_3 powder at 1000°C or heating GaN powders at 950°C. The products prepared from the later reaction consists of very long single crystalline Ga_2O_3 nanobelts and microscale single crystalline Ga_2O_3 sheets.
24. R. S. Wagner, W. C. Ellis, *Appl. Phys. Lett.* **4**, 89 (1964).
25. T. J. Trentler *et al.*, *Science* **270**, 1791 (1995).
26. G. W. Sears, *Acta Metall.* **3**, 268 (1956).

8 December 2000; accepted 1 February 2001